Oxide chemistry and local structure of PbZr$_x$Ti$_{1-x}$O$_3$ studied by density-functional theory supercell calculations

Ilya Grinberg, Valentino R. Cooper, and Andrew M. Rappe*

Department of Chemistry and Laboratory for Research on the Structure of Matter, University of Pennsylvania, Philadelphia, Pennsylvania 19104-6323, USA

The PbZr$_x$Ti$_{1-x}$O$_3$ (PZT) disordered solid solution is widely used in piezoelectric applications due to its excellent electromechanical properties. The disorder is caused by the random arrangement of B cations. To understand the relationship between properties of constituent atoms, local structure, and compositional phase transitions, we examine the response of the individual Pb atoms, B cations, and oxygen cages to the variation in the Zr/Ti arrangement and composition through first-principles density-functional-theory (DFT) calculations on a variety of PZT supercells. We use a statistical analysis of the relaxed DFT structures to identify crystal chemical structural motifs present in the Zr-rich rhombohedral, 50/50 monoclinic, and Ti-rich tetragonal phases of PZT and to examine the influence of composition variation on the motifs. We find that the distortions of the structure away from the ideal perovskite structure are governed by an interplay of bonding, electrostatic, and short-range repulsive interactions that depends on the B-cation arrangement. For Pb-atom displacements, there is a competition between electrostatic and bonding interactions that favor ordered collinear displacements, and local repulsive interactions that favor disorder. This competition is strongly affected by the changes in Zr/Ti composition and leads to compositional phase boundaries in PZT.

I. INTRODUCTION

The PbZr$_x$Ti$_{1-x}$O$_3$ (PZT) solid solution is a technologically important piezoelectric due to its superior electromechanical properties, which have only been recently surpassed by single-crystal piezoelectrics such as PMN-PT.[1] PZT has therefore been a focus of intense investigation experimentally and theoretically.[2-19]

PZT is a perovskite alloy of PbZrO$_3$ (PZ) and PbTiO$_3$ (PT). The end members of the PZT phase diagram, PZ and PT, have been characterized experimentally[10,20] and by means of theoretical DFT calculations.[21,22] PT is a ferroelectric (FE) material with a simple tetragonal structure, while PZ has a complex antiferroelectric (AFE) ground state. By themselves, neither PZ nor PT are particularly good piezoelectrics, but mixing these materials in a disordered solid solution gives rise to excellent piezoelectric response. The macroscopic phase of PZT depends on the Zr/Ti ratio and temperature. Six phases have been observed: a Zr-rich phase (AFE), two rhombohedral (R) phases at different temperatures (FE), a tetragonal (T) phase (FE), a paraelectric high-temperature cubic phase, and the recently discovered low-temperature monoclinic (M) phase (FE) around the 50/50 Zr/Ti composition[11,23] (the morphotropic phase boundary between the T and R phases).

All PZT phases are generated by distortions from the cubic perovskite structure, with a B cation in the center of the cube, O ions at the face centers of the cube, and Pb ions in the cube corners. The main difference between the phases lies in the lattice parameters and in the orientation of average polarization. For all phases, there is also variation in the magnitude and direction of the B-cation distortions within their O$_6$ octahedra, as well as in the magnitude and direction of the displacements of both the Pb and O ions away from

their perfect perovskite positions. This can be seen from the broadened peaks in the experimentally determined PZT neutron-scattering pair distribution functions[10] (PDF) (Fig. 1). It is this local disorder within the framework of the orderly perovskite lattice that gives PZT its interesting properties.

The M phase can be considered a bridge between the T and R phases, existing in a fairly narrow composition range (from 46% to 52% Ti) and showing a rapid change in lattice parameters with composition. The macroscopic polarization rotates from (100) at 52% to (111) at 46% and is approximately (211) at the 50/50 technologically most favorable composition. More recently, M phases have been observed in a variety of other Pb-based perovskites.[24-27]

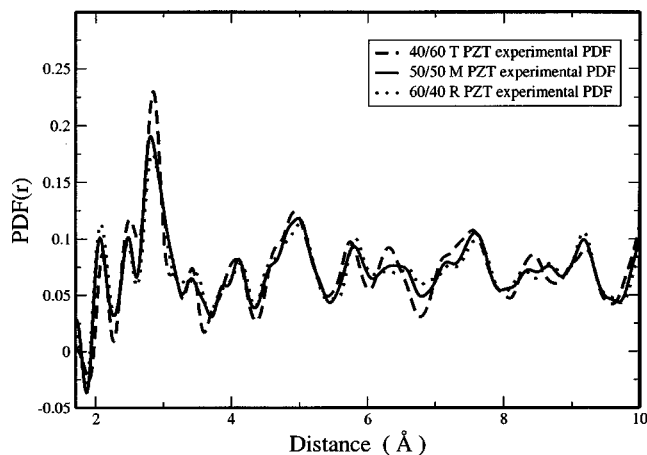In the past decade, neutron-scattering experiments[8,10,28]

FIG. 1. Experimental neutron-scattering pair-distribution functions (PDF's) for the T (dashed), M (solid), and R (dotted) phases of PZT from Dmowski *et al.* (Ref. 10).

have determined some structural features of PZT and related perovskite compounds. In $PbTiO_3$, Pb off-centers by 0.5 Å, making four short 2.5 Å Pb-O bonds. Ti off-centers by 0.3 Å, creating one very short 1.74 Å Ti-O bond. In the AFE PZ, four short Pb-O bonds are created by a combination of $Zr-O_6$ octahedral rotations and small Pb distortions. The motif of short Pb-O bonds is also present in PDF's of PZT at all compositions and in PDF's of many other Pb-based perovskites;[28] this seems to be an intrinsic requirement of the Pb-O bonding at the perovskite A site. Further experimental[12,29–31] and theoretical[4] studies have shown that octahedral rotations are not limited to the AFE end member PZ, but also exist in the FE R and M phases of PZT. In a low-temperature neutron-scattering PDF study,[10] Dmowski *et al.* have shown that in contrast to PZ and PT, the 60/40 R, 50/50 M, and 40/60 T phases of PZT display strong structural disorder in the atomic positions of the Pb atoms. The disorder is maximal at the 50/50 composition. While the assignment of the peaks in the PDF's puts a strong constraint on the Zr-O, Ti-O, Pb-O, and O-O distances, it does not uniquely determine the structure, since the PDF is an ensemble average over many local environments. All the phases have extremely similar PDF's, indicating similar local structure despite different orientation of overall polarization.

We note here that the chemistry of the A- and B-site off-centering has been shown to be different. The Pb displacement and the formation of short Pb-O and Pb-S bonds is driven by mixing of Pb $6s$ and $6p$ orbitals and O $2p$ states leading to the formation of a lone pair.[32,33] The off-centering on the B site is driven by hybridization between the B cation d states and the O $2p$ states,[34] which reduces the overlap repulsion, allowing for the formation of short B-O bonds.

Relating the origin of compositional phase transitions and morphotropic phase boundaries to properties of individual atoms is crucial for understanding the effect of variation in atomic composition on material properties. Such microscopic understanding is needed for the design of better materials and is most naturally obtained from first-principles calculations where one can, in a controlled way, vary the local structure of the material.

However, the study of disordered solid solutions such as PZT from a first-principles perspective is challenging for several reasons. PZT exhibits quenched disorder in the B-cation arrangement, creating a "disorder gap" between small, density-functional theory (DFT)-accessible supercells and the real material. The long-range Coulomb interactions of the charged ions in the system enable long-range structural correlations. Furthermore, as can be seen from the broad peaks in the experimentally obtained PDF's, a variety of distortions away from the high-symmetry positions are possible.

To bridge the disorder gap, we systematically examine the response of the Pb atoms, B cations, and O cages to variations in the Zr/Ti arrangement and composition through first-principles DFT calculations on a series of PZT supercells. A predictable dependence of motifs on local structure then allows construction of a conceptual framework that relates the microscopic changes in local structure with macroscopic compositional phase transitions.

The rest of the paper is as follows. In Sec. II we describe our methodology, both the computational techniques used to obtain the structures of PZT and the crystal-chemistry concepts that are used to analyze those structures. In Sec. III, a statistical analysis of the local structure of PZT is presented for O cages, B cations, and Pb distortions. In Sec. IV, we show how the motifs analyzed in Sec. III can be used to explain the distortions away from the high-symmetry structure observed in our PZT supercells. In Sec. V, we compare our supercells to the experimental PDF data for the R, M, and T phases of PZT. In Sec. VI, we show how changes in local structure with Zr/Ti composition are related to the compositional phase transitions. Section VII presents our conclusions.

II. METHODOLOGY

A. Crystal chemical analysis tools

The quenched disorder in the B-cation arrangement eliminates translational symmetry in PZT. This makes a real-space, local-structure-based treatment well suited for the analysis of the structure of this material. The crystal-chemistry approach treats atoms as distinct entities which possess transferable properties (e.g., atomic size). In a complex oxide such as PZT, optimal values for all atomic properties often cannot be achieved simultaneously, and the material assumes a compromise structure with tradeoffs among the various atoms. In this paper, we use crystal-chemical concepts to analyze the relaxed structures of our DFT supercells, relating the local structure in the supercells to atomic properties. We also analyze the behavior of each ion in terms of local structural motifs, analogous to the treatment of shell structures in fluids.

Ionic size is one of the simplest crystal-chemistry concepts. It is very useful for predicting bond distance and can also be used to predict ferroelectricity in perovskite materials. For example, for each ion, Shannon and Prewitt assigned a particular ionic size[35] (dependent on the coordination number); preferred distances between two nearest-neighbor ions can then be estimated by adding up their ionic radii. In the perovskite ABO_3 structure, the A-O and B-O sublattices have their own preferred bond lengths and lattice parameters. In some cases such as $PbTiO_3$, the preferences of the two sublattices nearly coincide. In other cases, the A-O sublattice would prefer either a shorter ($PbZrO_3$) or a longer ($BaTiO_3$) lattice constant than the B-O sublattice. In such cases, the actual lattice parameters assumed by the material are a compromise between the two preferences. To characterize the A-O/B-O competition in perovskites, the tolerance factor t is defined as

$$t = \frac{R_{\text{A-O}}}{R_{\text{B-O}}\sqrt{2}}, \quad (1)$$

where $R_{\text{A-O}}$ is the sum of A and O ionic radii and $R_{\text{B-O}}$ is the sum of B and O ionic radii. Tolerance factor $t<1$ leads to the rotation of the $B-O_6$ octahedra, accommodating the larger B-O sublattice by expansion of $B-O_6$ octahedra and accommodating the smaller A-O sublattice by shrinking the volume

TABLE I. Bond valence parameters for Pb-O, Zr-O, and Ti-O bonds given by Brown (Ref. 36) and as modified by us (Ref. 38).

	Brown's R^0	N	Modified R^0	N
Pb-O	2.044	5.5	2.021	5.5
Zr-O	1.950	6.0	1.937	6.0
Ti-O	1.806	5.2	1.846	5.2

of the A site. Such octahedral rotations often generate a low-temperature AFE phase (e.g., $PbZrO_3$). If $t>1$, the $B\text{-}O_6$ octahedra are stretched from their preferred B-O bond lengths, promoting B-cation distortions by creating room for the B cations to off-center. Therefore, simple perovskites with $t>1$ are usually FE. In the case of perovskites with mixed ion occupation on the B site, the $B\text{-}O_6$ octahedra of the larger B cation will be larger than those of the smaller B cation.

Another crucial crystal-chemical concept is valence.[36,37] Each atom in the system is viewed as seeking to possess the number of bonds equal to its formal charge (two for Pb and O, and four for Zr and Ti in PZ and PT). Since bond order is a function of the bond distance, some cation-anion distances may be shortened or lengthened to preserve the correct number of cation-anion bonds. A structure with atoms whose total bond orders are less than (underbonded) or greater than (overbonded) their valence is unfavored. The relationship between bond order and bond distance and consequent bonding requirements can be estimated from A-O and B-O distances in AO and BO_2 (for B cations with a valence of 4) oxides, respectively. For example, Pb-O bond lengths in PbO are about 2.5–2.7 Å; in a variety of FE, AFE, and relaxor perovskites, Pb-O distances are typically 2.85 Å in the high-symmetry structure. Pb atoms are underbonded in the high-symmetry structure, so they must make several short Pb-O bonds to satisfy the valence requirement. This results in the well-known tendency of Pb atoms to strongly off-center in a variety of perovskites.[28]

Empirically derived Brown's rules of valence[36] can be used to quantify bonding requirements for a range of oxide systems. Each atom has a desired valence (or total bond order) V_i^0. The actual valence of each ion can be calculated as a sum of individual cation-anion bond orders which are expressed as a power law in the bond distance R_{ij}. The deviation from the ideal valence V_i^0 for ion i is

$$\Delta V_i = \sum_j (R_{ij}/R_{ij}^0)^{-N_{ij}} - V_i^0. \tag{2}$$

The j sum runs over all nearest neighbors of the ith atom and R_{ij}^0 and N_{ij} relate bond strength to distance. If $\Delta V_i < 0$, the atom is underbonded, and $\Delta V_i > 0$ signifies overbonding. In this paper, we use the modified Brown's rules of valence R_{ij} and N_{ij} parameters[36,38] to analyze cation-oxygen bonding. Table I presents the original Brown's parameters for Pb-O, Ti-O, and Zr-O bonds and the parameters used here. The differences between the two parameter sets are slight. Empirical model calculations using the modified bond-valence

TABLE II. Distances and bond orders of the six shortest Zr-O bonds in PZ and Ti-O bonds in PT. Zr-O distances are from Teslic and Egami (Ref. 20); Ti-O distances are from Dmowski *et al.* (Ref. 10). All distances in Å. Bond orders are computed using the modified Brown's rules of valence (Refs. 36 and 38).

	Zr-O bond distance	Zr-O bond valence	Ti-O bond distance	Ti-O bond valence
x short	2.08	0.65	1.78	1.20
y short	2.08	0.65	1.98	0.70
z short	2.11	0.60	1.98	0.70
x long	2.10	0.62	2.37	0.29
y long	2.11	0.60	1.98	0.70
z long	2.15	0.60	1.98	0.70

(BV) parameters were able to correctly reproduce the compositional phase transitions and the neutron-scattering PDF's for the R, M, and T phases,[38] and we therefore used the modified set to perform the BV analysis.

While the concepts of ionic size and valence are general to a very wide class of materials, in this work we also extensively analyze the behavior of Pb and B-cation distortions inside their respective oxygen cages which is specific to FE perovskites. Cationic off-center distortions displace the center of positive charge with respect to the center of negative charge, giving rise to spontaneous macroscopic polarization. For the $B\text{-}O_6$ complexes, off-centering can be either covalent or transverse. In a covalently polarized $B\text{-}O_6$ complex, the B-cation displaces strongly toward one or more oxygen atoms, creating short covalent B-O bonds and splitting the $B\text{-}O_6$ distances into groups of short, medium, and long. In transversely polarized $B\text{-}O_6$ complexes, there is no B-cation displacement and the bond order of B-O bonds does not change from the ideal structure. Instead, the O_6 cages distort, changing the O-B-O angles and moving the center of the negative charge away from the B-cation position. This creates a local dipole moment transverse to the B-O bonds that participate in the angle bend. $Ti\text{-}O_6$ octahedra in PT are an example of covalent off-centering, while $Zr\text{-}O_6$ octahedra in PZ show transverse off-centering. The six shortest Zr-O and Ti-O distances in PZ and PT, respectively, are presented in Table II. The difference between the bond order of the shortest and longest Zr-O bonds is 0.12. For Ti-O, the bond order varies by 0.9, showing much greater covalency. The covalent distortion along the i direction D_i^c is given by

$$D_i^c = (R_i^{O1} + R_i^{O2})/2 - R_i^B, \tag{3}$$

where R_i^{O1} and R_i^{O2} are the coordinates along the i direction of the two oxygen atoms bonded to the B cation along the i direction and R_i^B is the i coordinate of the B cation. The total off-centering distortion D_i^t along the i direction is

$$D_i^t = \left(\sum_j R_i^{Oj} \right) \bigg/ 6 - R_i^B, \tag{4}$$

where the j runs over the six-nearest-neighbor oxygen atoms of the B cation.

Another motif specific to FE materials is the preference for the cationic distortions to align. In a study of prototypical ferroelectrics $BaTiO_3$ and $PbTiO_3$, Cohen showed that a delicate balance exists between long-range Coulomb interactions that favor FE distortions and the short-range repulsions which favor the undistorted high-symmetry structure. In BT and PT, the short-range repulsions are weakened by B-O and A-O hybridization, enabling cation distortions and giving rise to ferroelectricity. Simple arguments suggest that the individual dipole moments created by cation off-centering prefer to align. This is supported by the ordered low-temperature structure of simple FE perovskites. However, in some cases the preference for dipole alignment is outweighed by local interactions and an AFE (e.g., PZ) or a ferrielectric (e.g., $Na_{1/2}Bi_{1/2}TiO_3$) phase is preferred.[39] The fact that in such systems the distortions are smaller than in ferroelectric perovskites is further evidence of the general preference for dipole alignment.

Similar to a fluid, there are many different local configurations which give rise to the macroscopic properties of a disordered PZT solid solution crystal. However, even for completely aperiodic systems, pair distribution functions can provide ensemble average information about the interatomic distances. This makes analysis of the PDF's a natural choice for study of PZT local structure. Inspection of the PDF's obtained by Dmowski *et al.* shows a Ti-O peak at 1.85 Å, a Zr-O peak at 2.0 Å, a Pb-O peak at 2.5 Å, and a mixed Pb-O, O-O peak at 2.88 Å. (The amplitudes of the experimental PDF's are modified by the neutron-scattering lengths and thermal width factors for the constituent atoms. For Ti, the scattering length is negative; this explains the negative amplitude of the Ti-O peak.) The splitting of the Pb-O peak is present in PDF's of many FE perovskites[28] and points to the presence of large Pb distortions in the material. The PDF peak widths are indicative of the large degree of disorder present in the material. A perfect perovskite crystal would give sharp peaks (see Fig. 2) at short distances, in contrast with the broad peaks present in the experimental PDF's. Since the experimental PDF's were obtained at 10 K, the broad peaks in experimental PDF's cannot be accounted for by thermal motion and are evidence of structural disorder. Complete knowledge of the structures of our DFT supercells allows us to augment the analysis of the total PDF's by computing partial PDF's for Pb-O, B-O, and Pb-B-cation distances. These provide insights into the local structure unavailable from the analysis of the total PDF.

B. Supercell modeling of quenched disorder

To model the quenched B-cation disorder in PZT and the local structural response to the B-cation arrangement, we use DFT supercells with a variety of B-cation arrangements. The supercells used in our calculations can be thought of as snapshots of small regions of the real disordered solution. For the 50/50 Zr/Ti composition, we study the ten possible distinct arrangements of the B cations (Fig. 3) in a $4 \times 2 \times 1$ supercell. To examine Zr-rich and Ti-rich PZT, we use three distinct $3 \times 2 \times 1$ supercells at 67/33 and 33/67 compositions, respectively (Fig. 3). The energies and polarization directions of the relaxed structures of our DFT supercells are shown in Table III. The small energy differences between the supercells imply that the arrangements studied here will all be present in the real material.

The $4 \times 2 \times 1$ and $3 \times 2 \times 1$ supercells used in this study have a one-unit-cell periodicity in the z direction. Such periodicity is of course absent in the real PZT. Also, certain local environments cannot be studied in a $4 \times 2 \times 1$ or a $3 \times 2 \times 1$ supercell, such as a Zr (Ti) cation surrounded by six Ti (Zr) neighbors. To make sure that the local motifs we found are transferable to larger cells, we performed calculations on three distinct $3 \times 2 \times 2$ 60-atom supercells at 50/50 composition. A comparison of results for displacement magnitudes, cage volumes, and valences obtained by $4 \times 2 \times 1$ calculations and $3 \times 2 \times 2$ calculations is presented in Table IV; it can be seen that the differences between 40- and 60-atom results are quite small. Similar results are also obtained for angle scatter for the two sets of calculations. An analysis of 40-atom structures relaxed at experimental lattice constants
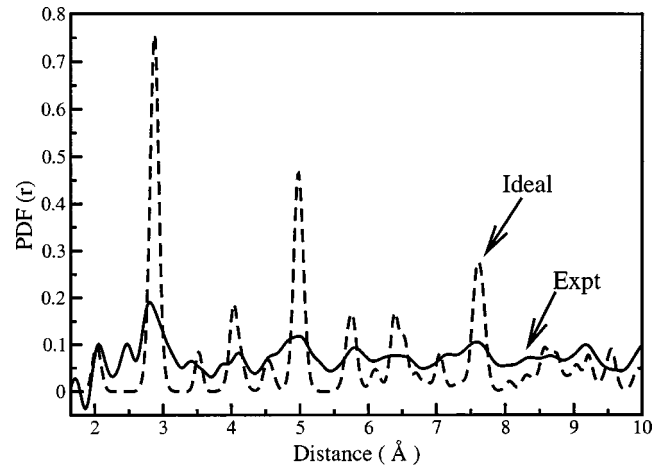

FIG. 2. Comparison of the experimental (Ref. 10) neutron-scattering PDF (solid) with that generated from an ideal perovskite structure (dashed) for 50/50 PZT. Note the much sharper peaks as well as the absence of a Ti-O dip at 1.85 Å and a Pb-O peak at 2.4 Å in the ideal perovskite.

	50/50				Ti-rich		
1	ZTZT TZTZ	6	ZZTT ZTTZ	1	TTT TZZ	2	TZT TZT
2	ZTZT ZTZT	7	TTZT ZZTZ	3	ZTT TZT		
3	ZZZZ TTTT	8	ZZTZ ZTTT		Zr-rich		
4	ZZTT ZZTT	9	ZTZT ZTTZ	1	ZZZ ZTT	2	ZTZ ZTZ
5	ZZTT TTZZ	10	ZZZT ZTTT	3	TZZ ZTZ		

FIG. 3. B-cation arrangements for 40-atom and 30-atom PZT supercells used in this work. Supercells 2 and 3 (40-atom) are related by a 90° rotation, but strain along the x axis breaks symmetry. Zr is denoted by Z; Ti by T.

TABLE III. Relative energies and directions of overall polarization for PZT supercells. For ease of comparison, all energies (even for the 30-atom supercells) are given in eV per 40-atom unit cell, relative to the lowest-energy supercell at each PZT composition.

	$c/a > 1$		$c/a = 1.0$	
	ΔE_{tot}	**P** direction	ΔE_{tot}	**P** direction
50/50				
Supercell 1	0.097	(100)	0.120	(111)
Supercell 2	0.051	(100)	0.165	(433)
Supercell 3	0.162	(621)	0.165	(343)
Supercell 4	0.110	(100)	0.180	(111)
Supercell 5	0.005	(632)	0.000	(111)
Supercell 6	0.075	(632)	0.066	(111)
Supercell 7	0.052	(922)	0.071	(111)
Supercell 8	0.118	(100)	0.272	(111)
Supercell 9	0.067	(100)	0.111	(111)
Supercell 10	0.075	(611)	0.127	(111)
Ti-rich				
Supercell 1	0.000	(100)		
Supercell 2	0.119	(100)		
Supercell 3	0.047	(100)		
Zr-rich				
Supercell 1			0.105	(433)
Supercell 2			0.285	(111)
Supercell 3			0.000	(455)

gives $18.5 \pm 14.4°$ for a Pb distortion angle off the (100) direction; the corresponding value for the 60-atom calculations is $22.2 \pm 14.5°$. The agreement between the 40- and 60-atom results indicates that despite the artificially short periodicity in the z direction, the results found for our 40- and 30-atom supercells are representative of the local structure of PZT and our DFT study identifies distortion patterns and correlations which are present in the real disordered material.

Other authors[2–6,16,19,40] have studied the relationship of strain and composition. We choose fixed lattice constants in

TABLE IV. Comparison of local motifs obtained from analysis of 60-atom and 40-atom 50/50 PZT structures. Displacements are in Å, volume in Å^3. Bond valences are computed using the modified Brown's rules of valence (Refs. 36 and 38).

	Average			
	Displacement	Percent covalency	O_6 volume	Bond valence
60-atom Pb	0.42			1.96
40-atom Pb	0.45			1.98
60-atom Zr	0.23	57	70.6	3.94
40-atom Zr	0.25	51	70.2	4.01
60-atom Ti	0.23	78	64.1	3.96
40-atom Ti	0.24	79	64.5	3.96
60-atom O				1.97
40-atom O				1.99

TABLE V. Energies and polarization directions for final structures of three different ionic minimizations for supercells 4, 5, and 6 at experimental volume and lattice constants. Energies in eV per 40-atom unit cell, relative to the lowest-energy supercell (see Table II).

	ΔE_{tot}	**P** angle away from (100)
Supercell 5		
Run 1	0.005	31°
Run 2	0.007	22°
Run 3	0.006	29°
Supercell 6		
Run 1	0.075	26°
Run 2	0.075	25°
Run 3	0.081	23°
Supercell 7		
Run 1	0.052	18°
Run 2	0.052	14°
Run 3	0.053	35°

order to focus on local structure. Since DFT calculations using the local-density approximation (LDA) tend to give errors of about 1% in the lattice constant and since ferroelectricity is sensitivity dependent on the volume of the material, we used the experimental volume for all calculations. For the 50/50 Zr/Ti calculations, we performed calculations both at the experimental 50/50 lattice constants ($a = 4.03$ Å, $c = 4.14$ Å) as well as at the cubic lattice constants ($a = 4.075$ Å) that would give experimental volume. For calculations at the experimental lattice constants, the (100) direction was chosen to be the c axis. Since the angles between the axes are very close to 90° for all PZT phases in this study, and since the a and b lattice constants are essentially identical, we use supercells whose lattice vectors are multiples of tetragonal primitive axes. The calculations for Ti-rich supercells were done at $c = 4.1758$ Å and $a = 3.992$ Å, and the calculations for the Zr-rich supercells were done at cubic lattice constant $a = 4.0835$ Å.

Relatively large and highly bonded systems such as our 40-atom supercells have large numbers of coupled degrees of freedom. The potential energy surface is complicated and it is reasonable to expect that several distinct low-energy distortion sets will be present. To explore this issue, we performed ionic minimization starting from three different sets of randomized perfect perovskite positions for the low-symmetry supercells 5, 6, and 7. Somewhat surprisingly, we find that despite different starting points, all runs finished with the same energy within 0.006 eV per 40-atom cell. The energies and the polarization directions for the three runs for supercells 5, 6, and 7 are presented in Table V. The structures are subtly different, but have similar overall polarization and follow the same pattern. Thus it seems that instead of several sharply defined, distinct minimum-energy structures, PZT supercells have one somewhat broad global minimum. This is in complete agreement with the finding that the ease of polarization rotation leads to superior electromechanical properties.[41] Our results indicate that the overall pattern of the local distortion is uniquely determined by the B-cation arrangement of the supercell.

C. Density-functional-theory computational method

The DFT calculations were performed with our in-house plane-wave code, using the local-density approximation[42,43] for the exchange-correlation functional. To represent the interactions of the nucleus and core electrons with the valence electrons, we use optimized norm-conserving pseudopotentials[44] and a 50 Ry cutoff, modified with the designed nonlocal approach[45] to achieve best transferability. The pseudopotentials are the same as those used in previous studies of PZT.[16] The electronic minimization was done using the blocked-Davidson iterative diagonalization[46,47] with Pulay density mixing.[48] For each B-cation configuration, we used randomized perfect perovskite coordinates as the starting point of the ionic minimization. These were generated by an addition of displacements between -0.5 and 0.5 Å to the x, y, and z ideal perovskite positions of each atom. The ionic minimization was performed without any symmetry constraints and all degrees of freedom were relaxed using a quasi-Newton algorithm.[49]

All calculations on $4 \times 2 \times 1$ supercells are done with $1 \times 2 \times 4$ Monkhorst-Pack k-point sampling of the Brillouin zone. At this k-point sampling, energy differences are converged within 6 meV per 40-atom supercell. For calculations on the 60-atom $3 \times 2 \times 2$ supercells we used a $2 \times 2 \times 2$ Monkhorst-Pack grid, and for $3 \times 2 \times 1$ supercell calculations a $2 \times 2 \times 4$ k-point sampling was used.

III. RESULTS—STATISTICAL ANALYSIS OF LOCAL STRUCTURE

We now analyze the relaxed structures of our DFT supercells to examine the effects of variation in composition and local B-cation arrangement on the local structure of PZT. We seek to understand if the local structure of PZT is a simple combination of PZ and PT or if the mixture of the two end members gives rise to new behaviors. We also examine the correlations between local B-cation arrangement and distortion magnitudes and directions of O_6 cages, B cations, and Pb atoms.

A. Oxygen cages

We find that the overall oxygen lattice framework is preserved even for disordered supercells. Therefore, to characterize the distortions of the oxygen atoms away from the perfect perovskite positions, we analyze the size and the tilt angle of the O_6 cages, examining the extent to which each octahedron acts as it does in the end-member compounds, and the extent to which the octahedra influence each other, giving rise to compromise behaviors.

For all supercells, we find that the Zr-O_6 octahedra expand from the ideal perovskite positions, with Zr-O_6 volumes of $68-72$ Å^3.[52] Conversely, because of the smaller size of the Ti ion, the Ti-O_6 octahedra contract, with Ti-O_6 volumes of $62.5-66.5$ Å^3 (Fig. 4). As can be seen from Fig. 4, there is no overlap in the size of the Zr-O_6 and Ti-O_6 octahedra; the smallest Zr-O_6 cage has a larger volume than the largest Ti-O_6 cage. The direction of the Zr (Ti) oxygen cage expansion (contraction) depends on the local B-cation ar-
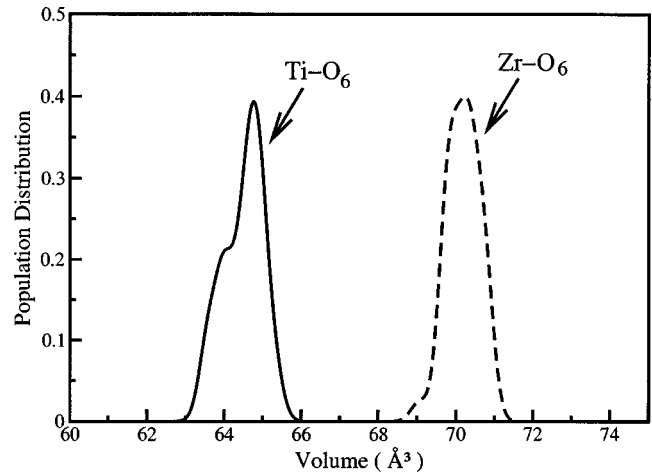

FIG. 4. Octahedral volumes for Ti (solid) and Zr (dashed) octahedra in PZT. T, M, and R phases exhibit the same range of volumes. The Ti ions always have smaller octahedral cages than the Zr ions.

rangement, with oxygen atoms moving about 0.1 Å away from the Zr ions and toward the Ti ions. In all cases, approximately the same octahedral volume will be achieved. The differences in the observed Zr-O_6 and Ti-O_6 volumes are consistent with the ionic size difference of the two B cations (ionic radius of 0.72 Å for Zr and 0.60 Å for Ti).

In addition to expansion and contraction, the oxygen octahedra also undergo slight rotations. While the O_6 tilting is absent in FE PT, PZ shows 14° tilts of Zr-O_6 complexes.[20,21] For monoclinic 50/50 PZT, octahedral rotations have been predicted theoretically[4] and found experimentally.[12,29–31] Figure 5 shows the octahedral tilting for the B-O_6 octahedra in our calculations for the three phases of PZT. In the monoclinic 50/50 phase, the majority of the octahedra tilt by less than 2°, although some tilts in the 3°–5° range are present. There is no significant difference in the amount of the tilting
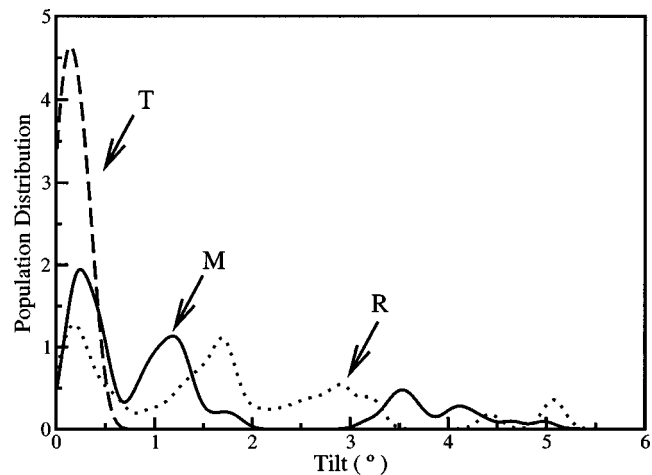

FIG. 5. Distribution of octahedral tilts away from the Cartesian axes for T (dashed), M PZT (solid), and R (dotted) PZT. The T structures exhibit very little octahedral tilting, while in R, PZT tilts are evenly distributed up to 5°. The majority of M PZT structures have tilts of less than 2°.
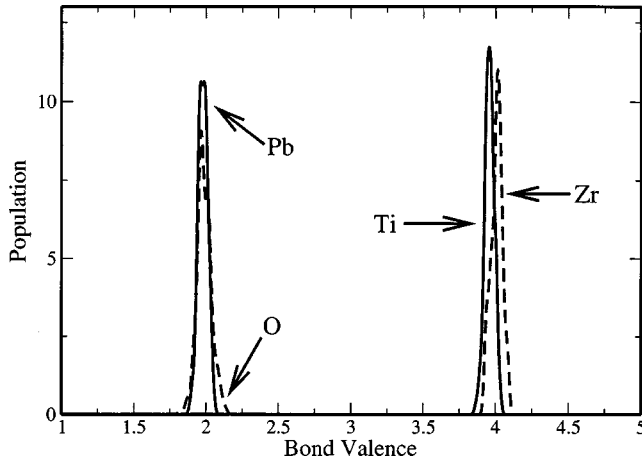
FIG. 6. Distribution of bond valence sums for Pb (solid), O (dashed), Ti (solid), and Zr (dashed) atoms obtained from the relaxed structures of DFT supercells.

of $Ti-O_6$ and $Zr-O_6$ complexes in B-cation environments with local 50/50 compositions. Most $Ti-O_6$ and $Zr-O_6$ complexes display a compromise tilting behavior, although the compromise is in favor of Ti, with small $0°-2°$ tilt. However, $B-O_6$ complexes in locally Zr-rich environments behave more like the $Zr-O_6$ complexes in PZ, accounting for the $3°-5°$ tilt population in Fig. 5.

Unlike the octahedral volume, the magnitude of the octahedron rotation is strongly affected by PZT composition. The Ti-rich phase displays almost no octahedral tilting, while in the Zr-rich phase, octahedral tilts are evenly distributed in the $0°-5°$ range. Although larger tilts are observed in phases with a higher composition of Zr, Ti octahedra show the same degree of tilting as the Zr octahedra for a given composition.

Calculation of oxygen atom valences provides strong validation of the bond valence approach. In PZT, each oxygen atom bonds with four Pb cations and two B cations. In an ideal perovskite structure, the valence rule is not satisfied. For example, at 50/50 experimental lattice constants, the oxygen atom valences can vary from 1.7 to 2.14, depending on the local B-cation arrangement. Nevertheless, in the relaxed structure, despite the presence of several types of bonds and a variety of local environments, oxygen atoms at all compositions have valences in a narrow range around 2.0 (Fig. 6). The small width of the oxygen peak in Fig. 6 (no underbonded or overbonded O atoms) indicates that the achievement of the ideal valence is a strong requirement of the O-atom bonding.

Our results show that ionic size is a transferable atomic property which is not affected by local environment. The $B-O_6$ cages achieve the desired volume by an anisotropic environment-dependent expansion or contraction. Rotational character is strongly affected by local environment, with the minority B cation taking on the characteristics of the majority B cation. Analysis of oxygen atom bonds in the framework of the bond valence theory shows that deviations from the ideal valence (underbonding and overbonding) are strongly disfavored for oxygen atoms in PZT.

TABLE VI. Average magnitude of Pb, Zr, and Ti distortion (in Å) away from the center of the oxygen cage for Zr-rich, 50/50, and Ti-rich PZT.

	Zr-rich 67/33 30-atom	50/50 40-atom	Ti-rich 33/67 30-atom
D_{Pb}	0.45 ± 0.04	0.44 ± 0.03	0.45 ± 0.03
D_{Zr}	0.23 ± 0.06	0.25 ± 0.04	0.33 ± 0.04
D_{Ti}	0.24 ± 0.06	0.24 ± 0.03	0.26 ± 0.04

B. B cations

To characterize B-cation behavior, we analyze the Zr/Ti-O bonding and B-cation displacements in the relaxed structure of our supercells. We compare the B-cation behavior at different compositions of PZT with the B-cation behavior in the end members PZ and PT.

An analysis of $B-O_6$ complexes shows that Zr and Ti bond valences in all three phases are very close to the ideal valence of 4. In a perfect perovskite structure, Zr is overbonded (4.4 for the 50/50 volume) and Ti is underbonded (3.66 for the 50/50 volume). This energetically unfavorable situation is relieved by the expansion (contraction) of Zr (Ti) O_6 cages. However, for the Ti atoms, the $Ti-O_6$ contraction does not fully eliminate underbonding. A Ti atom located in the center of an O_6 cage with a volume of 16 $Å^3$ would have a bond valence of only 3.86. Therefore, an off-center distortion is necessary to achieve the desired ideal valence of 4.0. Off-center displacements for Zr and Ti are also favored by the long-range electrostatic interactions.

We now examine B-cation distortions. We find that in PZT, both Zr and Ti move off-center by 0.2–0.3 Å and create short Ti-O and Zr-O bonds at all compositions (Tables VI and VII and Fig. 7), making an important contribution to the overall polarization. Similar results have been found by Fornari and Singh.[4] The magnitude of Ti distortion is the same for all three compositions, whereas Zr distortions show an increase on going from the 50/50 to the Ti-rich composition. The angular distributions of Zr and Ti distortion directions (Figs. 8 and 9) are similar to each other for any one compo-

TABLE VII. Typical distances and bond orders of the six shortest Zr-O and Ti-O bonds in 50/50 PZT at experimental volume and lattice constants ($a = 4.03$, $c = 4.14$). All distances in Å. Bond orders are computed using the modified Brown's rules of valence (Refs. 36 and 38).

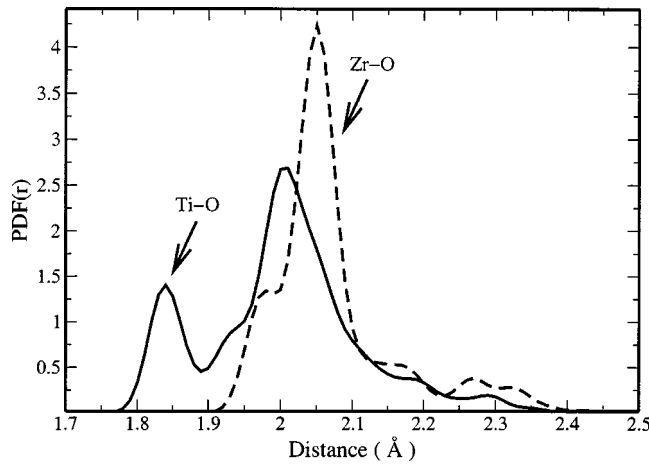|	Zr-O bond distance	Zr-O bond valence	Ti-O bond distance	Ti-O bond valence
x short	1.984	0.865	1.822	1.071
y short	2.028	0.759	1.939	0.775
z short	2.058	0.696	1.999	0.660
x long	2.214	0.449	2.358	0.279
y long	2.118	0.586	2.027	0.614
z long	2.086	0.641	2.067	0.555

FIG. 7. Ti-O (solid) and Zr-O (dashed) partial PDF's calculated from the relaxed structures for the 50/50 experimental lattice constant supercells.

sition, but exhibit large variations between the compositions. For the Ti-rich PZT, all B-cation distortions are in a very narrow range along the (100) direction, while a broad range of distortion directions is seen for the 50/50 and especially the Zr-rich PZT. However, even for the Zr-rich composition, we find that all B-cation distortions lie in a 40° cone around the overall (111) polarization direction, with no distortions having ($\bar{1}00$), ($0\bar{1}0$), or ($00\bar{1}$) components. Such alignment of the distortions is evidence of an electrostatic dipole-dipole interaction between the local dipole moments created by the B-cation distortions.

Examination of the Ti-O and Zr-O bond distances in the B-O_6 complexes shows that there are differences in the directionality of the Zr-O and Ti-O bonding. In 50/50 PZT, most (87%) Ti atoms make a very short 1.80–1.85 Å Ti-O bond with one oxygen atom, although some (12%) Ti atoms have three short distances in the 1.90 Å range. Zr-O bonding is less directional, with two or three short 1.97–2.03 Å Zr-O bonds. The preference of Zr to form two or three strong Zr-O bonds, versus the preference of Ti to make one very strong Ti-O bond, is due to the greater polarizability of Zr.
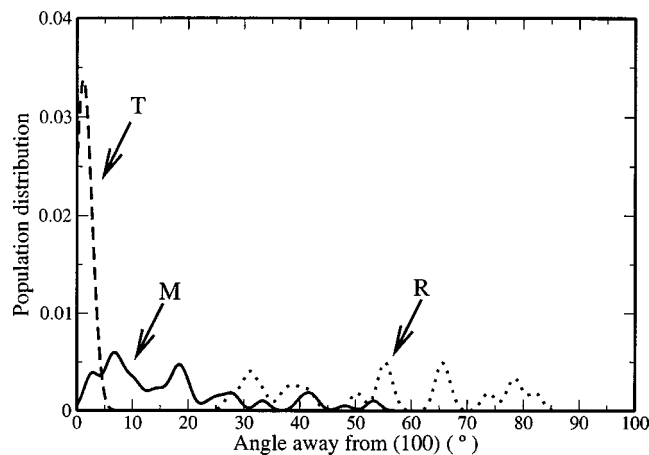
FIG. 8. Distribution of B-cation distortion angles away from the (100) direction for T (dashed), M (solid), and R (dotted) PZT.
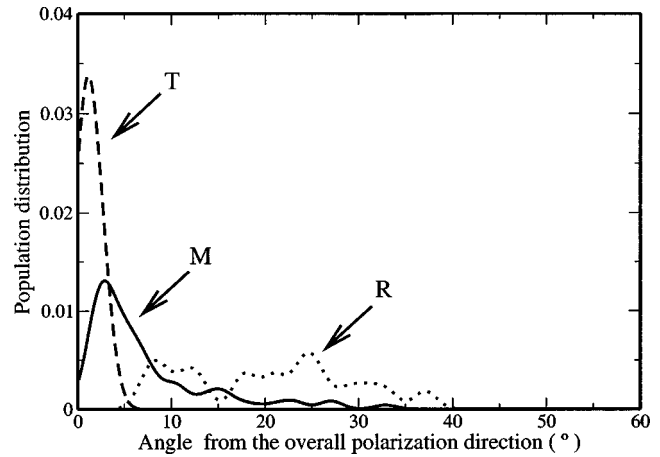

FIG. 9. Distribution of B-cation distortion angles away from overall polarization direction of the supercell for T (dashed), M (solid), and R (dotted) PZT.

Another difference between the two ions lies in the character of off-center distortion. Zr distortions are consistently less covalent than Ti distortions, with Ti covalency of 72–82 % and Zr covalency of 48–59 % (Figs. 10 and 11). The larger fraction of the covalent off-centering for Ti is a consequence of Ti underbonding in the center of its O_6 cage. This makes the formation of short cation-oxygen bonds with large bond order favorable. For Zr-O_6 there is progression from the average distortion covalency of 47% in the 67/33 Zr-rich phase to 54% covalency in the 50/50 phase and 60% covalency in the 33/67 Ti-rich phase. Since in the parent compounds, Ti favors covalent off-centering and Zr favors transverse off-centering, in PZT the replacement of Zr-O_6 with Ti-O_6 decreases the number of neighbors that can accommodate bond bending. This makes transverse distortions less favorable and increases the covalency of Zr-O_6 distortions. A similar trend can be observed for Ti-O_6 covalency character.

Similarly to the B-O_6 octahedra, the B-cation distortions display a mix of transferable and environment-dependent properties. While Zr and Ti valences and the magnitude of Ti distortions in PZT are intrinsic B-cation features, the magnitude of Zr distortions and the covalency character are environment-dependent. The formation of very short Ti-O bonds of high bond order can be traced to the underbonding of the Ti in the center of its O_6 cage; the absence of corresponding short Zr-O bonds is due to the lack of such underbonding for the Zr atoms. The amount of B-cation distortion direction scatter is strongly dependent on composition. However, strong dipole alignment interactions are evident for all three PZT compositions.

C. Pb atoms

To examine Pb-atom behavior, we first analyze the Pb distortions and Pb-O bonding in PZT and compare them to those in PZ and PT. In all three phases of PZT studied here, we find strong Pb off-centering distortions of 0.45 Å (Table VI), which creates short Pb-O bonds in the Pb-O_{12} complex. The creation of short Pb-O bonds is necessary to satisfy the
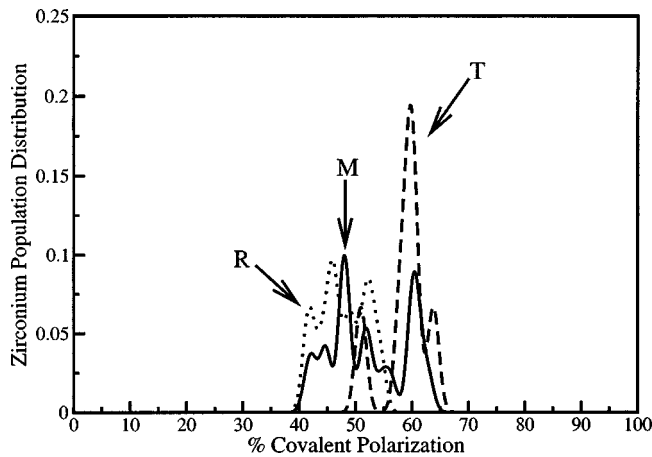
FIG. 10. Covalency character of Zr polarization for *T* (dashed), *M* (solid), and *R* (dashed) PZT. The *T* phase, which displays less tilting, has a more covalent nature to its polarization, while the more tilted *R* phase shows less covalency. Structures with more freedom to rotate exhibit a smaller degree of covalent polarization.

Pb valence of 2, since in the ideal perovskite structure (with 12 Pb-O bonds of 2.88 Å) the Pb valence is only 1.8. The large distortions found in our PZT calculations are much more similar to the large 0.5 Å Pb distortion found in PT than to the small Pb distortions of approximately 0.2 Å found in PZ.

Despite strong similarities in Pb distortion magnitude and creation of short Pb-O bonds for all compositions, there are significant differences in the directions of Pb distortions and the distribution of Pb-O bond distances in the Pb-O_{12} complex. There is a progression from order to disorder in these degrees of freedom from the Ti-rich to the 50/50 to the Zr-rich composition, as can be seen from the Pb-O partial PDF's presented in Fig. 12.

The sharp peaks of the Ti-rich Pb-O PDF are due to a clear division of the Pb-O distances into groups of nearly identical short, medium, and long bonds created by distortion
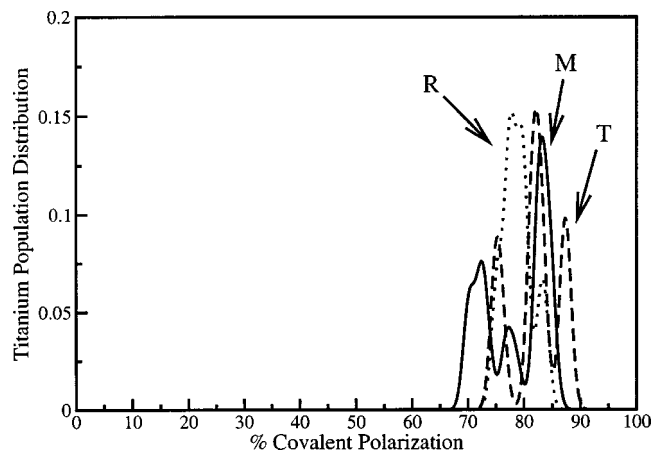

FIG. 11. Covalency character of Ti polarization for *T* (dashed), *M* (solid), and *R* (dotted) PZT. The *T* phase, which displays less tilting, has a more covalent nature to its polarization, while the more tilted *R* phase shows less covalency. Structures with more freedom to rotate exhibit a smaller degree of covalent polarization.
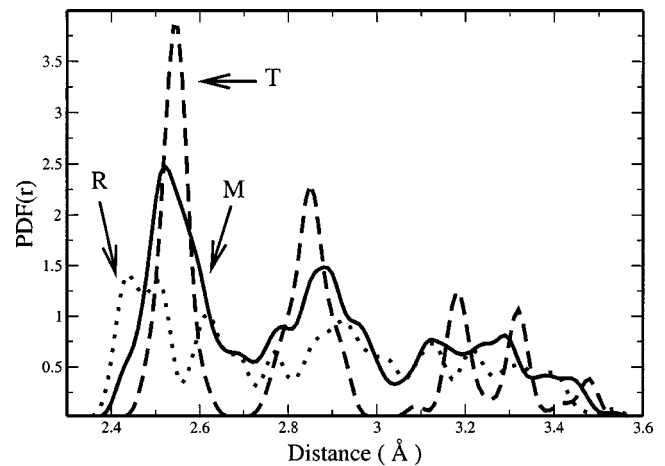

FIG. 12. Pb-O partial PDF's for the *T* (dashed), *M* (solid), and *R* (dotted) PZT calculated from relaxed supercell structures.

along the (100) direction. This is similar to the (100) distortions of Pb atoms in PT. The broad peaks of the Zr-rich Pb-O partial PDF are due to a continuous range of Pb-O distances in the Pb-O_{12} complex. Such a range of Pb-O distances cannot be created by (100) distortions, but must be due to distortions along a variety of low-symmetry directions close to (110), similar to the (110) distortions found in PZ. (A (111) distortion would create well-defined sets of three short, six medium, and three long Pb-O distances.) The 50/50 composition displays a Pb-O PDF between the Zr-rich and the Ti-rich compositions, indicating Pb distortion directions between those of Zr-rich and Ti-rich compositions.

Direct examination of the angular distribution of the Pb distortion directions (Figs. 13 and 14) confirms our analysis
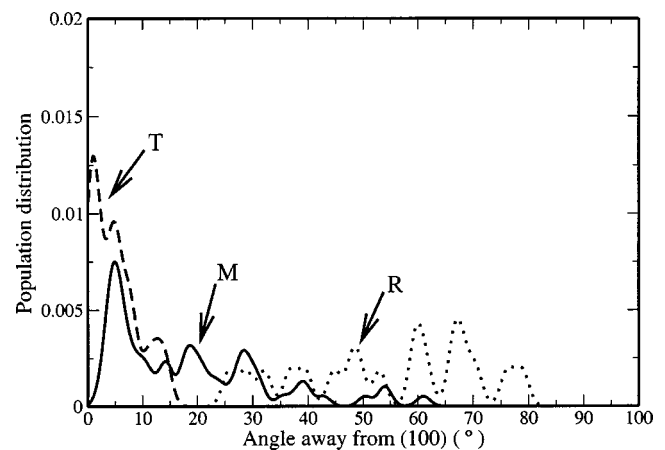

FIG. 13. Distribution of B-cation distortion angles away from the (100) direction for *T* (dashed), *M* (solid), and *R* (dotted) PZT. Pb distortions at 33/67 composition do not deviate more than 15° away from the (100) direction, therefore giving rise to a *T* phase. Pb distortions at the 67/33 composition show significant deviation (40°–60°) away from the (100) direction, indicating the presence of an *R* phase. Pb distortions at the 50/50 composition display deviations mostly in the 0°–45° range, with some deviations of up to 60°, indicating an overall (211) direction of polarization and an *M* phase.
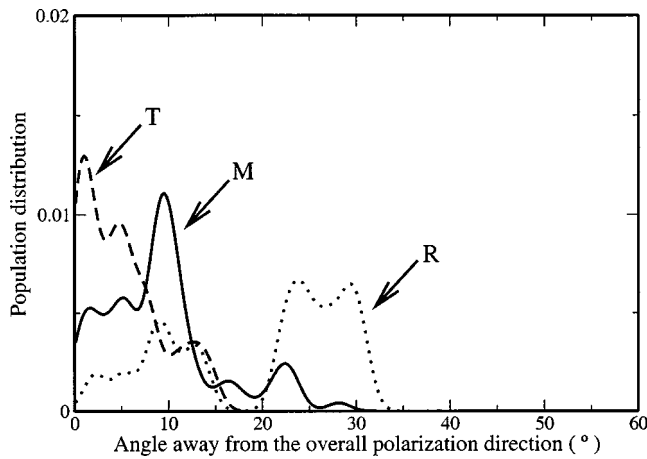
FIG. 14. Distribution of Pb distortion angles away from overall polarization direction of the supercell for T (dashed), M (solid), and R (dotted) PZT.
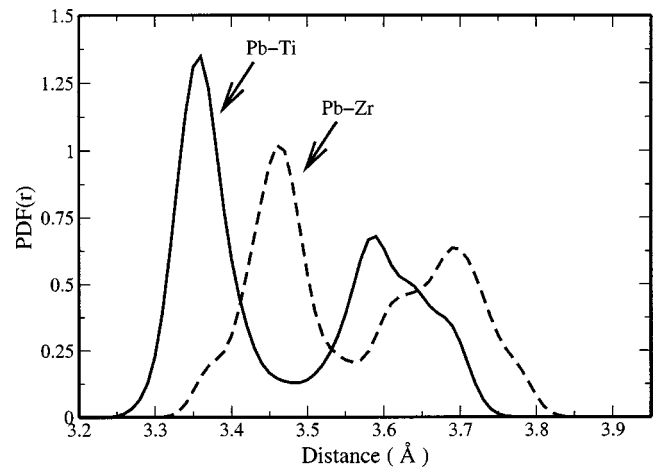

FIG. 15. Pb-Ti (solid) and Pb-Zr (dashed) partial PDF's obtained from the relaxed structures of the 50/50 PZT supercells at experimental lattice constants.

of the Pb-O partial PDF's. The Ti-rich composition PZT has no Pb distortions with more than a 15° deviation away from the [100] ferroelectric direction. On the other hand, in the Zr-rich composition, the Pb displacement angles are broadly distributed between 30° and 80° away from the [100] direction. The 50/50 composition is the bridge between the Zr-rich and Ti-rich compositions, with some population of Pb distortion angles between 0° and 15° (similar to the Pb distortion angles found in Ti-rich PZT), some population between 35° and 65° (similar to the Pb distortion angles found in the Zr-rich PZT), and some population in the intermediate 15°–30° range found only in the 50/50 composition.

Pb atom distortions display greater sensitivity to the variation in the local environment than the B-cation distortions. A comparison of the angular distribution of the Pb distortion directions and the B-cation distortion directions (Figs. 8 and 9) shows that for the Zr-rich and the 50/50 compositions there are only very minor differences in the angular distributions of the Pb distortions and the B-cation distortions. However, for the Ti-rich phase, the B-cation distortions are located within a very narrow range of less than 5°, indicating essentially no deviation from the (100) overall polarization of the material. The range of Pb distortion angles is three times larger, with a significant population in the 10°–15° range, indicating a tilting of the Pb distortions away from the (100) direction in response to the local environment.

The greater sensitivity of the Pb atoms is due to the fact that the anisotropy created by the disordered Zr/Ti arrangement is stronger for the Pb local environment than for the B-cation environment. In the ideal perovskite structure, both Pb and B cations have a symmetrical nearest-neighbor oxygen shell. For Pb, symmetry is broken in the second-nearest-neighbor shell formed by the Zr and Ti cations in a disordered arrangement. For Zr and Ti, the second-nearest-neighbor shell is formed by identical Pb atoms and Zr/Ti disorder breaks symmetry in the third-nearest-neighbor shell.

We now examine the nature of the Pb-B interactions. In PZT, Pb, Zr, and Ti atoms are all positively charged and this gives rise to a Pb-B-cation repulsion. Evidence of such repulsion can be seen from the broad angular distributions of

the Zr-rich composition. Pb distortions along the (111) direction bring a Pb atom directly toward a B cation and are not particularly favorable (in fact there is a dip at 54° in Fig. 13 and 0° in Fig. 14, corresponding to the (111) direction), even though the overall polarization direction is (111).

While analysis of Pb-O PDF's and Pb distortion angular distribution elucidates the overall trends in Pb-atom behavior with composition, an examination of partial Pb-Zr and Pb-Ti PDF's (Fig. 15) calculated from 50/50 supercells at the experimental lattice constants can shed light on differences in the Pb-Zr and Pb-Ti repulsive interactions and the consequent response of the Pb distortions to the variation in the local B-cation arrangement. The Pb-Ti PDF displays a sharp peak at 3.32 Å; the Pb-Zr PDF exhibits a more diffuse peak at 3.5 Å. The differences in the position of the two peaks indicate that Pb atoms either displace away from neighboring Zr atoms toward neighboring Ti atoms or make smaller distortions to avoid the creation of unfavorable short Pb-Zr distances. The small variation in the Pb distortion magnitudes implies that the tilting of Pb distortions away from Zr and toward Ti is the more common Pb response to the presence of Zr atoms.

The differences in the location and the width of the Pb-Zr and Pb-Ti peaks are consistent with crystal-chemical ideas of ionic size and hardness. Zr has a larger ionic radius than Ti (0.72 versus 0.60 Å) and this leads to a greater repulsion between the positive Pb and Zr ions than between the Pb and Ti ions. This leads to larger average distance for Pb-Zr than for Pb-Ti. The $3d$ valence electrons of Ti make it a hard ion and create a hard-wall-like repulsive interaction between Pb and Ti atoms. Zr is more polarizable than the Ti, and therefore the repulsion turns on more slowly (albeit at larger distances than that of Pb-Ti), resulting in a more diffuse first Pb-Zr peak.

Our examination of the Pb atom behavior shows that the need to create short Pb-O bonds to satisfy the Pb valence requirement leads to large Pb distortions of essentially the same magnitude at all three PZT compositions. However, the analysis of bond distances in the Pb-O_{12} complexes shows a
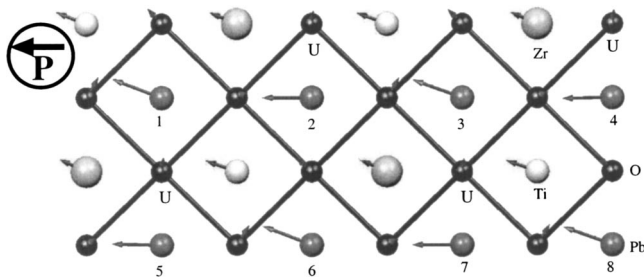
FIG. 16. Projection of the structure of supercell 1 at experimental lattice constants on the *x-y* plane. Arrows (with a scale factor of 4) show the displacements from perfect perovskite positions.

progression from the PT-like to PZ-like Pb-O_{12} complexes and distortion directions with increasing Zr concentration, and a corresponding progression from structural order to disorder as exhibited by the partial Pb-O PDF's and Pb distortion angle distributions. Pb distortions also exhibit a sensitivity to local structure variation, leading to a preference of Pb atoms to displace toward Ti cations and away from Zr cations. This is easily understood as a consequence of the difference in the ionic sizes of the two B cations.

IV. LOCAL MOTIFS AND SUPERCELL STRUCTURES

A. Distortion analysis

We now show how the distortions found in our relaxed DFT supercells satisfy the preferences of Pb and O atoms and B cations examined in Sec. III. In some cases, the preferences of Pb and O atoms and B cations (such as the need to achieve the desired valence and ionic size, minimize Pb-B-cation repulsion, and align dipole directions) can be simultaneously satisfied. In other cases, they conflict, and the local structure of the material is a compromise between the interactions. Whether there is a conflict or cooperation among the various motifs is sensitively dependent on the B-cation arrangement of the supercell.

We use supercells 1, 3, 5, and 6 at experimental (Figs. 16–19) lattice constants as examples for 50/50 PZT. Supercells 1 and 3 are high-symmetry, (110) and (100), stackings in the Zr/Ti arrangement, respectively, and can be represented by 10-atom supercells. The high symmetry of B-cation arrangement in these supercells simplifies the analysis of the structural distortions. For the Ti-rich and Zr-rich compositions, we examine the structures of the lowest-
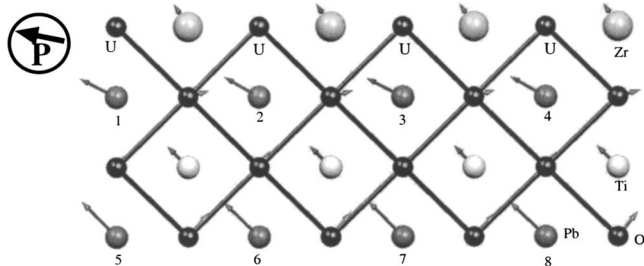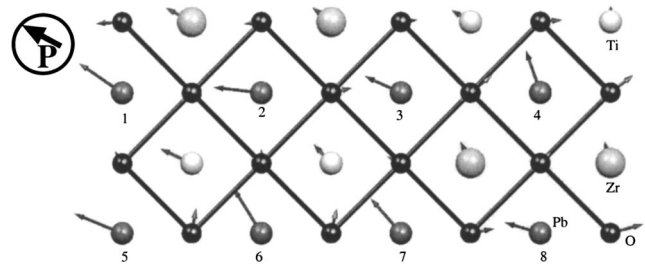
energy DFT supercell (Figs. 20 and 21). Since there is no variation in the B-cation arrangement along the *z* axis, Figs. 16–21 show projections of the relaxed structures on the *xy* plane.

The structure of supercell 1 nicely illustrates bond valence conservation, ionic size difference effects, and Zr/Ti distortion character differences found by statistical analysis in the previous section. Desired valences are achieved for Pb atoms by large Pb distortions, and for the B cations by a combination of expansion (contraction) of the Zr (Ti) O_6 complexes and B-cation distortions. For the oxygen atoms marked U, the Pb distortions away from the Zr ions create a depletion of Pb-O bond order. The Pb-O underbonding is compensated by strong distortions of the neighboring Ti atoms, creating 1.84 Å Ti-O bonds with a bond order of 1.0. The effects of the ionic size difference of Zr and Ti are apparent in the zigzag pattern of Pb distortions. The zigzag is not large, since the local Pb preference to move away from Zr is balanced by the electrostatic interactions and the preference for dipole alignment. The insensitivity of the B cations to their local environment means that the dipole alignment preference is dominant and all B cations move in the same direction.

The structure of supercell 3 is a good example of how the delicate balance between the various interactions can influence orientation of the overall polarization. At first glance, one might expect a pattern of Pb-atom displacements with small tilts away from Zr atoms and toward Ti atoms and (100) B-cation distortions due to a balance between the local repulsion and dipole alignment, leading to overall polarization along the (100) direction. However, the Pb-Zr repulsion is stronger for this supercell than for supercell 1 due to the
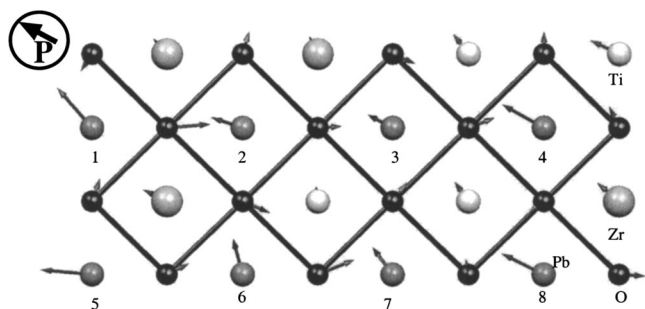

FIG. 18. Projection of the structure of supercell 5 at experimental lattice constants on the *x-y* plane. Arrows (with a scale factor of 4) show the displacements from perfect perovskite positions.

FIG. 17. Projection of the structure of supercell 3 at experimental lattice constants on the *x-y* plane. Arrows (with a scale factor of 4) show the displacements from perfect perovskite positions.

FIG. 19. Projection of the structure of supercell 6 at experimental lattice constants on the *x-y* plane. Arrows (with a scale factor of 4) show the displacements from perfect perovskite positions.
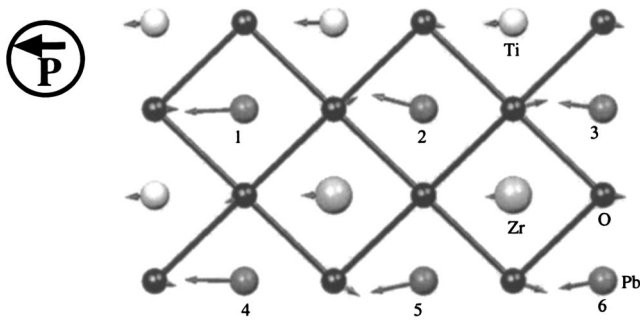
FIG. 20. Projection of the structure of the lowest-energy Ti-rich supercell on the x-y plane. Arrows (with a scale factor of 4) show the displacements from perfect perovskite positions.
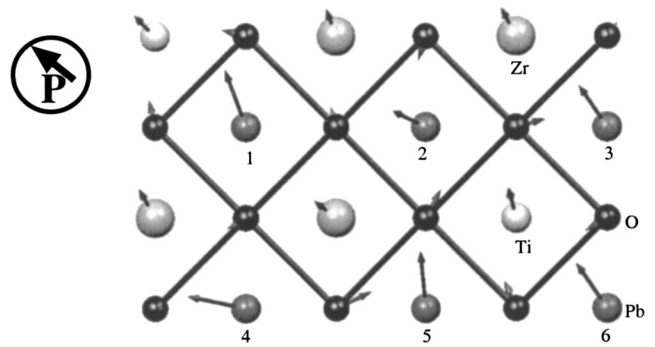

FIG. 21. Projection of the structure of the lowest-energy Zr-rich supercell on the x-y plane. Arrows (with a scale factor of 4) show the displacements from perfect perovskite positions.

presence of an all-Zr plane, leading to stronger conflict between dipole alignment and local preferences. A set of Pb distortions along the (100) direction with tilts toward Ti would also lead to a decrease in Pb-O bond order for the oxygen atoms marked U in supercell 3. In supercell 1, the Pb-O bond depletion for oxygen atoms marked U was compensated by the formation of a Ti-O bond with high bond order; here the oxygen atoms in the top row have Zr neighbors, for which the low covalency character of distortions disfavors the formation of a single very short Zr-O bond.

To avoid underbonding and to minimize dipole scatter, the supercell adopts a structure with overall (621) polarization. Once again, we see that the B cations display smaller scatter in the distortion direction than the Pb atoms. The Pb atoms in the bottom row distort away from Zr and toward Ti atoms and satisfy both the dipole alignment and local repulsion preferences. For the Pb atoms in the top row, the dipole alignment preference is satisfied but the preference to avoid Zr atoms is not, as short (3.35 Å) Pb-Zr distances are created by the Pb distortions. The strong conflicts between the various interactions in this structure make supercell 3 the highest energy supercell.

The lower symmetry B-cation arrangement of supercell 5 is more typical of real PZT and leads to a more disordered structure, with distortion directions that are sensitive to the local B-cation arrangement. Similarly to supercell 3, a structure with strong Pb tilts away from Zr and toward Ti and an overall (100) polarization is not favorable in supercell 5, due to the creation of underbonded and overbonded oxygen atoms and large dipole scatter. Instead, the supercell assumes a monoclinic structure.

The directions of Pb distortions display a striking correlation with the local B-cation environment. All Pb atoms have significant distortion components along the x axis; this brings Pb atoms closer to the Zr and Ti cations located to the left (in a (100) face) and increases the distances between the Pb atoms and the Zr and Ti cations located to the right (in a ($\bar{1}$00) face). Therefore, the arrangement of Zr and Ti cations in the (100) face plays a primary role in determining the directions of Pb-atom distortions. In the top row of Pb atoms, Pb atoms 1 and 4 displace away from the Zr atoms in their (100) faces, creating a strong positive y distortion component. Pb atoms 2 and 3 cannot avoid their (100) face Zr atoms by distortions with a strong negative y component,

since that would lead to unfavorable dipole scatter and the creation of underbonded and overbonded oxygen atoms, as in the case of supercell 3. The competition between the interactions leads to compromise displacements mostly along the x axis for Pb atoms 2 and 3.

The arrangement of the Zr and Ti cations in the ($\bar{1}$00) face is a secondary influence on the Pb distortion directions. For Pb atom 4, an upward displacement moves the Pb atom away from both Zr atoms below; for Pb atom 1, an upward displacement moves the Pb atom away from the Zr atom in the (100) face but toward the Zr atom in the ($\bar{1}$00) face. Therefore, the Pb atom 4 distortion has a larger y component (0.325 Å) than the Pb atom 1 distortion (0.247 Å). Similarly, due to the presence of a Ti atom in the ($\bar{1}$00) face, a positive y distortion component is more favorable and is larger for Pb atom 3 (0.111 Å) than for Pb atom 2 (0.040 Å).

Supercell 6 is a good example of how the Pb atoms in 50/50 PZT respond to the presence of locally Zr-rich B-cation environments. Here, a structure with (100) polarization and little dipole scatter would create high Pb-Zr repulsion. A structure in which all Pb atoms satisfy their preference to avoid Zr atoms would have to exhibit a very large dipole scatter with ($\bar{1}$00) distortion components for Pb atoms 2 and 6. Instead, supercell 6 assumes a compromise monoclinic structure. A combination of small Pb displacements and larger than usual Zr-O$_6$ tilt creates short Pb-O bonds for Pb atom 2 and a large (010) distortion component reduces the Pb-Zr repulsion for Pb atom 6.

For Ti-rich PZT supercells, the lack of conflict between local Pb-B repulsion preference and bond valence conservation and dipole alignment interactions leads to more ordered structures. The supercell shown in Fig. 20 exhibits a highly ordered structure with average 5.5° Pb distortion deviation from the overall (100) polarization direction and all B-cation distortions exactly along (100). It is interesting to compare this structure to the structures of 50/50 supercells 1 and 5. The tilts away from the Zr atoms are clearly much smaller than those in 50/50 supercell 5, which also has a B-cation arrangement with two Zr atoms in a row, and the zigzag pattern of the Ti-rich composition is actually more similar to the distortions in 50/50 supercell 1. In the Ti-rich supercell, the absence of Zr neighbors in the (100) face for Pb atoms 1 and 4, and longer Pb-Zr distances created by large Zr distor-

TABLE VIII. Pb displacements (in Å) in the lowest-energy Zr-rich supercell.

	x	y	z	Total
Pb 1	0.21	0.30	0.24	0.44
Pb 2	0.09	0.36	0.39	0.47
Pb 3	0.43	0.08	0.22	0.49
Pb 4	0.22	0.27	0.27	0.44
Pb 5	0.28	0.08	0.31	0.42
Pb 6	0.12	0.39	0.26	0.48

tions, diminish Pb-Zr repulsion strength. Therefore, large Pb distortion tilts away from Zr atoms are not necessary to avoid short Pb-Zr distances and high Pb-Zr repulsion and the local repulsion and dipole alignment preferences can be simultaneously satisfied.

For Zr-rich PZT supercells, we find that the conflict between the various preferences is exacerbated by the dominance of Zr-rich local environments, leading to highly disordered structures. For example, the structure of the lowest-energy 67/33 Zr-rich supercell (Fig. 21) has large angle scatter in the cation distortions. The polarization is rhombohedral (111), but as the data in Table VIII show, only some of the Pb atoms actually off-center along the (111) direction, as that would incur a high Pb-Zr repulsion energy cost. (The Pb atoms that do off-center along (111) are permitted to do so by a strong B-cation distortion.) Instead, Pb atoms move in a variety of directions toward the available Ti atoms. While the scarcity of Ti atoms favors large variations in Pb distortion directions, all distortions are limited to the (111) octant by the need to satisfy dipole alignment and bond valence preferences.

Our examination of PZT supercells shows that the cationic distortion directions are determined by a complex interplay of bonding, electrostatic, and local repulsion interactions. Dipole alignment and avoidance of oxygen underbonding or overbonding favor an ordered structure, while the local Pb-B repulsion-based preferences favor more scatter in the distortion direction. For 50/50 PZT, B-cation arrangement has a strong effect on the balance of various interactions; this gives rise to structures of different polarization orientation and degree of order in the 50/50 supercells. For Ti-rich supercells, local Pb-B repulsions are weaker, and this leads to an ordered (100) phase for all supercells. In the Zr-rich supercells, increased strength of Pb-B repulsion leads to a disordered compromise phase with an average polarization along (111).

B. Energy differences

The assignment of energy differences between the supercells to particular local motifs is difficult due to the complicated interplay of interactions and the small magnitude of the energy differences. Nevertheless, for some cases, the variation in the degree of conflict and cooperation among the local structure motifs can be directly related to the DFT energy differences.

For example, as mentioned above, for the 50/50 PZT supercells, the high energy of supercell 3 is due to large frustration present in that supercell. For the Ti-rich composition, the presence of an all-Zr face along the (100) direction in supercell 2 leads to a conflict between the preference of Pb atoms to distort along the (100) directions and a high Pb-Zr repulsion that is incurred by such distortions. Therefore, supercell 2 is the highest-energy Ti-rich supercell. For the Zr-rich supercells, dispersion of Ti atoms makes it easier to simultaneously satisfy local repulsions and distortion alignment preferences, and therefore supercell 3 is preferred. In supercell 2, two Pb atoms are surrounded by Zr neighbors only. For these Pb atoms, the achievement of an ideal valence and distortion alignment preferences are in sharp conflict with the preference to avoid the short Pb-Zr distances and high Pb-Zr repulsion. This leads to the high energy of Zr-rich supercell 2.

The magnitudes of DFT energy differences for the three compositions studied are consistent with the transition from ordered structures with weak conflict on the Ti-rich side to disordered compromise structures with strong conflict on the Zr-rich side. The data in Table III show that the spread in supercell energy differences is 0.119 eV for the Ti-rich composition, 0.162 eV for the 50/50 composition, and 0.285 eV for the Zr-rich composition. As Zr content is increased, the degree of conflict between the preferences becomes more sensitive to the exact details of the B-cation arrangement and this leads to a larger energy variation for the Zr-rich supercells.

Examination of the energy difference between the experimental and cubic lattice constants reveals that the energy cost of polarization rotation to the (111) direction depends on the polarization orientation at experimental lattice constants. For the 50/50 supercells polarized along a low-symmetry direction, the energy cost to transform to cubic lattice constants and a (111) orientation of polarization is on average only 12 meV. The corresponding cost of the 50/50 supercells polarized along the (100) direction is much higher, 81 meV. For the lower symmetry supercells, many cation distortions are in between (100) and (111). Upon rotation to overall (111) polarization, the distortion directions change somewhat, but the satisfaction of local preferences is not significantly disturbed. For the (100) polarized supercells, moving to a (111) overall polarization strongly disrupts the satisfaction of local preferences, raising the cost of the polarization rotation.

While the exact energy values for interactions such as dipole alignment, bond valence satisfaction and Pb-B-cation repulsion cannot be determined from the energy differences presented here, correlations are present between the B-cation arrangement and the resultant tradeoffs between the satisfaction of various preferences and the energy of the supercells. A larger degree of conflict between the motifs in a supercell leads to a higher energy for that supercell. This is particularly pronounced for the Zr-rich composition, as the conflict between dipole alignment and bond valence preference on one hand and the local Pb-B repulsion preference on the other hand is especially strong due to the scarcity of the Pb-friendly Ti cations.
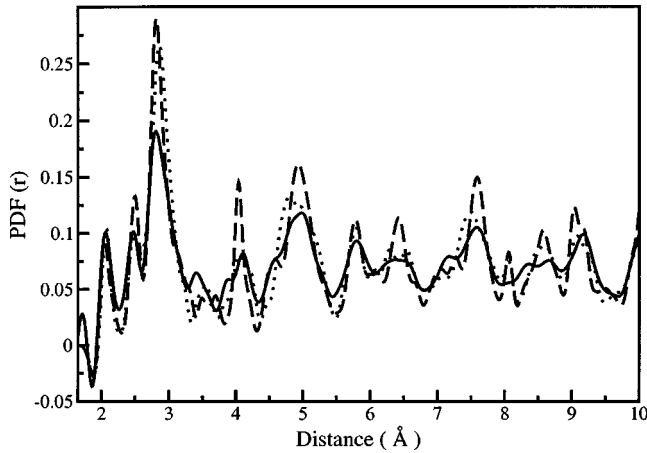
FIG. 22. Neutron-scattering PDF's obtained by experiment (Ref. 10) (solid) and calculated from the relaxed DFT 40-atom (dashed) and 60-atom (dotted) supercell structures for 50/50 monoclinic PZT.

V. COMPARISON WITH EXPERIMENTAL PDF

To make contact with experimental results, we compare average PDF's generated from our calculated minimum-energy DFT structures with the experimentally obtained PDF's.[10] Figure 22 shows the PDF calculated for the 50/50 monoclinic phase of PZT. Although the peaks in the DFT-based PDF are too narrow (due to the small size of the supercell), they are otherwise in excellent agreement with the experimental PDF. The sharp peaks at approximately 4 and 8 Å are artifacts created by the short periodicity of our $4 \times 2 \times 1$ supercells. The agreement between experiment and the 60-atom DFT PDF's is better, reflecting the better representation of the disordered B-cation arrangement in the 60-atom calculations as well as the presence of B-cation environments impossible to represent in the $4 \times 2 \times 1$ supercells (such as a Ti cation surrounded by six Zr cations).

Figure 23 shows the PDF's calculated for the T phase. Here the peaks are even sharper than for 50/50 PDF, reflecting the high order of the structures obtained by DFT for 30-atom supercells and the ordered nature of the Ti-rich te-
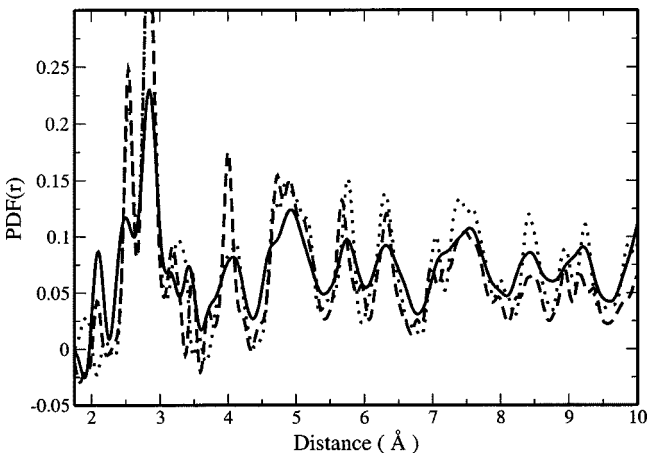

FIG. 23. Neutron-scattering PDF's obtained by experiment (Ref. 10) (solid) and calculated from the relaxed DFT 30-atom supercell (dashed) and 60-atom (dotted) structures for T PZT.

tragonal PZT. Interestingly, for the Zr-rich 67/33 supercells (Fig. 24), the peak widths as well as the peak positions agree very well with the experimental 60/40 PDF (besides the artifact at 4 Å for the 30-atom PDF). The fact that such a small snapshot accurately captures the disorder in the material is striking evidence of the short-range disorder and compromise nature of the R phase.[8,10,38]

The absence of splitting in the Zr-O peak in experimental and theoretical PDF's (Figs. 22–24) seems to indicate that ferroelectric Zr distortions in PZT are small. The well-known tolerance factor argument (see Sec. II) also predicts a lack of Zr ferroelectricity as the tolerance factor between Pb-O and Zr-O bonds is less than 1. This is in disagreement with large Zr distortions actually found in our DFT calculations (Table VI) as well as in the DFT calculations of Fornari and Singh.[4]

The discrepancy between the small tolerance factor of PZ and lack of Zr-O splitting in the PDF's on one hand, and ferroelectric distortions by Zr atoms found by DFT calculations on the other hand, can be resolved as follows. The tolerance factor argument is valid for PZ, where each Zr ion is in an isotropic environment surrounded by other Zr ions, and the octahedral cage is therefore the same in all three Cartesian directions. However, in PZT, the presence of Ti ions creates anisotropy in the Zr-ion environment and in the dimensions of the Zr-O_6 octahedra, as the Zr-O_6 octahedra expand in the direction of neighboring Ti atoms. Some of the O-Zr-O octahedral axes are longer than in PZ, creating room for Zr ion distortion. The strong off-centering of the Pb and Ti ions also favors formation of short Zr-O bonds and a strong Zr distortion. These two effects counter the Pb-O and Zr-O sublattice mismatch (small tolerance factor) and make ferroelectric Zr distortions possible in PZT. This is particularly pronounced in Ti-rich PZT, where an abundance of Ti neighbors and a large c/a ratio give rise to especially large (0.33 Å) Zr off-centering.

The absence of a splitting in the Zr-O PDF is due to the smaller differences in bond length between the short and medium Zr-O bonds and a distribution of short and medium Zr-O bond lengths in the 1.97–2.05 Å range. This range is due to variation in the local Zr octahedral sizes created by a disordered Zr/Ti arrangement. Disorder also leads to significant variation in the length of the long Zr-O bonds, giving rise to a long tail in the Zr-O partial PDF.

A comparison of the six shortest Zr-O distances in the relaxed structures of supercell 1 and supercell 2 at experimental lattice constants (Table IX) provides a good example of the effect of Zr environmental anisotropy on Zr distortions. The B-cation arrangements of the two supercells are related by a 90° rotation; however, the presence of a strain along the x axis breaks the symmetry. In both supercells, the largest polarization component is along the x axis. In supercell 1, the Zr-O_6 expansion creates an O-Zr-O distance of 4.3 Å along the x axis. This allows a very long 2.33 Å Zr-O distance, giving rise to a 0.352 Å difference between the short and long Zr-O bonds along the x axis with a difference of 0.55 in Zr-O bond order. In supercell 2, the Zr-O_6 octahedra do not expand along the x axis (since their neighbors along x are other Zr atoms), and O-Zr-O distance is therefore only 4.15 Å. The absence of favorable coupling between
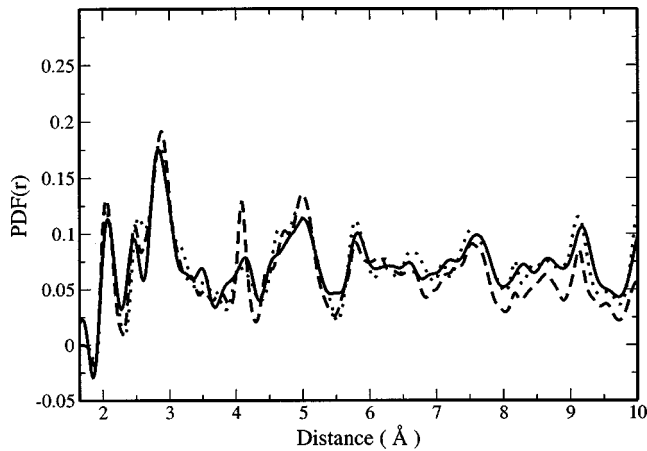
FIG. 24. Neutron-scattering PDF's obtained by experiment (Ref. 10) (solid) and calculated from the relaxed DFT 30-atom supercell (dashed) and 60-atom (dotted) structures for *R* PZT.

TABLE IX. Distances and bond orders for the typical six shortest Zr-O bonds in supercell 2 and supercell 3. All distances in Å. Bond orders are computed using the modified Brown's rules of valence parameters (Refs. 36 and 38).

	Zr-O in supercell 1		Zr-O in supercell 2	
	Bond distance	Bond valence	Bond distance	Bond valence
x short	1.976	0.886	1.972	0.898
y short	2.049	0.714	2.054	0.703
z short	2.050	0.711	2.026	0.764
x long	2.328	0.333	2.181	0.490
y long	2.058	0.696	2.147	0.536
z long	2.059	0.694	2.062	0.688

strain and Zr/Ti arrangement diminishes ferroelectric activity, leading to a smaller Zr off-centering.

Our DFT calculations reproduce experimental PDF's, especially for the larger 60-atom cells. However, the ability of DFT calculations to obtain detailed microscopic information on specific local environments reveals surprising information, such as the ferroelectric activity of the Zr cation, impossible to obtain from the ensemble-averaged experimental PDF data.

VI. LOCAL STRUCTURE AND PHASE TRANSITIONS

From the structural motifs presented above, a common theme emerges in the behavior of the oxygen octahedra and the cation distortions. We can separate the local motifs into the intrinsic crystal-chemistry requirements which are independent of the environment, and the nontransferable ways to achieve these intrinsic requirements. For example, the Zr oxygen cages and the Ti oxygen cages prefer a certain volume (around 70 Å for Zr-O_6 and around 64 Å for Ti-O_6) in all environments. However, the actual octahedral distortion that achieves the desired volume depends on the local B-cation arrangement, and the disorder in the B-cation arrangement gives rise to a variety of anisotropic B-O_6 octahedra. Both Zr and Ti ions polarize significantly in all environments, but the role of covalent versus transverse polarization depends on the Zr/Ti composition, with the majority B cation inducing the minority B cation to acquire more of its behavior. All Pb atoms distort by 0.4–0.5 Å (this is also seen in other Pb-based perovskites),[28] however the direction in which Pb atoms distort depends on the details of the local B-cation arrangement and the overall polarization of the material.

The Pb off-centering behavior is governed by several interactions. An analysis of experimental PDF's (Fig. 1) and our calculations (Fig. 12) shows that in all PZT phases, Pb atoms make short Pb-O bonds. Pb atoms prefer distortions toward a (100), (010), or (001) face, forming the required short, covalent Pb-O bonds with four nearest-neighbor oxygen atoms, to distortions along (111) directions, forming the

covalent Pb-O bonds with three nearest-neighbor oxygen atoms. While a Pb move along (111) satisfies the Pb-O bonding requirement, the short Pb-B distance causes a strong Pb-B repulsion. As discussed in Sec. III, the Pb atoms prefer to off-center toward the face that is closest to the overall polarization direction, avoiding the large Zr cations and moving toward the smaller Ti cations as much as possible. Pb atoms make strong distortions toward Ti-rich (0 or 1 Zr) faces, sometimes with a small tilt away from the Zr or toward the overall polarization direction. Pb atoms also displace toward neutral faces (2 Zr and 2 Ti), but with significant tilts away from Zr atoms. Zr-rich (3 or 4 Zr) faces cause the Pb to either move toward a different face or to reduce Pb distortion magnitude significantly. In all-Zr local environments, a significant (greater than 5°) octahedral rotation brings some of the oxygen atoms closer to the high-symmetry Pb position; this reduces the magnitude of Pb distortion necessary for the creation of the required short Pb-O bonds.

We now examine how the interplay of the electrostatic dipole interactions and local A-B cation repulsion gives rise to compositional phase transitions. The relative amounts of Zr-rich, neutral, and Ti-rich faces are strongly dependent on Zr/Ti composition, as shown in Fig. 25. At very low Ti content, most of the Pb atoms are located in all-Zr local environments. In such environments, due to a scarcity of small Ti ions, a large ferroelectric Pb distortion would incur a large local repulsion energy cost. Instead, large octahedral rotations bring O atoms close to Pb, requiring only a small (0.1–0.2 Å) Pb distortion to form short Pb-O bonds.[20,21] A rotation of one octahedron leads to rotation of the neighboring octahedron in the opposite direction; this doubles the unit cell and results in antiferroelectricity.[50] The need to avoid the large local repulsion wins over the preference for dipole alignment, resulting in an antiferroelectric phase.

As Ti content is increased, the percentage of the all-Zr environments declines rapidly, decreasing the local repulsion energy of a disordered ferroelectric rhombohedral phase. The decrease in local repulsion energy and the replacement of the Zr-O_6 octahedra with more ferroelectric Ti-O_6 octahedra makes dipole alignment favorable, and PZT undergoes an AFE-FE compositional phase transition. However, the domi-
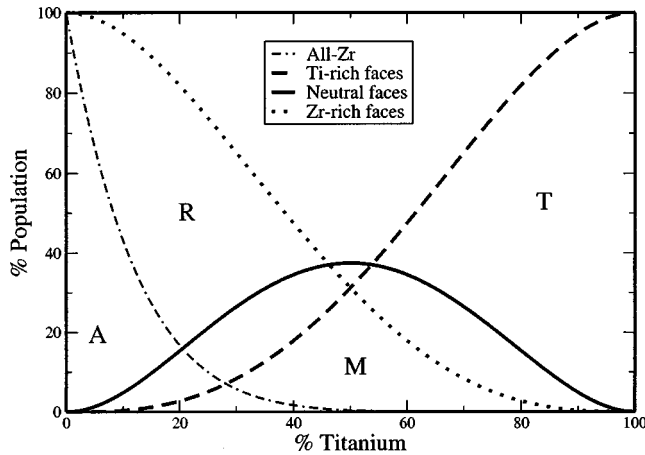
FIG. 25. Populations of various Pb environments in PZT as a function of Ti composition. *A*, *R*, *M*, and *T* denote the locations of the antiferroelectric, rhombohedral, monoclinic, and tetragonal PZT phases at low temperature.

nance of the Zr-rich environments drives ferroelectric Pb distortions in any direction that would give a longer Pb-Zr distance, creating an overall (111) polarization, with a large scatter in the directions of cationic displacements. In the rhombohedral phase, a compromise is reached between the dipole-dipole interactions and the local Pb-B repulsion interaction.

In the monoclinic phase at around the 50/50 composition, some of the environments unfavorable to tetragonal distortion are replaced with neutral or Ti-rich ones, due to larger Ti content. This allows some of the Pb distortions to rotate toward the (100) direction, lowering the energy due to smaller scatter away from the overall polarization direction. However, since around 30% of Pb atoms are located in environments unfavorable to tetragonal distortion, polarization rotation leads to a monoclinic phase and not a tetragonal one.

On the Ti-rich side of the phase diagram, the (100) distortion satisfies the local energy preferences of most Pb atoms, and those with an unfavorable environment are forced to have a considerable component of distortion in the (100) direction, because of the substantial energy lowering due to the alignment with the strong overall (100) polarization. In the tetragonal phase, especially at very high Ti content, both the dipole alignment and the local repulsion preferences are satisfied.

Phase diagrams of perovskite solid solutions made by mixing an antiferroelectric such as PZ with PT, or a relaxor[53]

ferroelectric such as PMN with PT, exhibit the same sequence of phase transitions with increasing Ti content: from parent antiferroelectric or relaxor ferroelectric, to a rhombohedral FE, to monoclinic FE, to a tetragonal FE phase.[24,25,51] If the rhombohedral phase were just as ordered as the tetragonal one, it is not obvious why (111) would be preferred at lower Ti concentrations. However, this general pattern can be easily understood in light of the fact that the rhombohedral phase is a disordered compromise structure between the dipole alignment and the local repulsion interactions. In an antiferroelectric or relaxor material, an ordered ferroelectric distortion pattern incurs too great a cost in local repulsion due to the large size of the B cations. As the smaller and more ferroelectric Ti cation is added, the local energy cost of ordered ferroelectricity is diminished and the material undergoes a series of phase transitions: first to the disordered rhombohedral FE phase, to a monoclinic phase, and then to an ordered tetragonal FE phase.

VII. CONCLUSION

We used DFT calculations to study the local structure of PZT in the Zr-rich rhombohedral, 50/50 monoclinic, and Ti-rich tetragonal phases. The effects of overall composition, local B-cation arrangement, and strain on local structure were examined. We find that well-known crystal-chemical concepts provide a good framework for understanding the interactions in PZT. The interplay between the preference to minimize dipole scatter and the A-B local repulsive interactions gives rise to the progression of phase transitions from AFE to *T* with increasing Ti content. We believe that this effect is not specific to PZT but is rather the underlying cause for phase transitions in other ferroelectric perovskite alloys.

*Corresponding author. Email address: rappe@sas.upenn.edu

[1] S.-E. Park and T. R. Shrout, J. Appl. Phys. **82**, 1804 (1997).

[2] D. Vanderbilt and M. H. Cohen, Phys. Rev. B **63**, 094108 (2001).

[3] G. Saghi-Szabo, R. E. Cohen, and H. Krakauer, Phys. Rev. B **59**, 12 771 (1999).

[4] M. Fornari and D. J. Singh, Phys. Rev. B **63**, 092101 (2001).

[5] L. Bellaiche and D. Vanderbilt, Phys. Rev. Lett. **83**, 1347 (1999).

[6] L. Bellaiche, A. Garcia, and D. Vanderbilt, Phys. Rev. Lett. **84**, 5427 (2000).

[7] P. Ghosez, E. Cockayne, U. V. Waghmare, and K. M. Rabe, Phys. Rev. B **60**, 836 (1999).

[8] D. L. Corker, A. M. Glazer, R. W. Whatmore, A. Stallard, and F. Fauth, J. Phys.: Condens. Matter **10**, 6251 (1998).

[9] A. J. Bell and E. Furman (unpublished).

[10] W. Dmowski, T. Egami, L. Farber, and P. K. Davies, in *Fundamental Physics of Ferroelectrics—Eleventh Williamsburg Ferroelectrics Workshop*, edited by R. E. Cohen (American Institute of Physics, Melville, NY, 2001), pp. 33–44.

[11] B. Noheda, D. E. Cox, and G. Shirane, Appl. Phys. Lett. **74**, 2059 (1999).

[12] A. G. Souza, J. L. B. Faria, P. T. C. Freire, A. P. Ayala, J. M. Sasaki, F. E. A. Melo, J. Mendes, E. B. Araujo, and J. A. Eiras, J. Phys.: Condens. Matter **13**, 7305 (2001).

[13] R. Guo, L. E. Cross, S.-E. Park, B. Noheda, D. E. Cox, and G. Shirane, Phys. Rev. Lett. **84**, 5423 (2000).

[14] J. A. Rodriguez, A. Etxeberria, L. Gonzalez, and A. Maiti, J. Chem. Phys. **117**, 2699 (2002).

[15] G. A. Rossetti, J. P. Cline, Y. M. Chiang, and A. Navrotsky, J. Phys.: Condens. Matter **14**, 8131 (2002).

[16] N. J. Ramer, E. J. Mele, and A. M. Rappe, Ferroelectrics **206**, 31 (1998).

[17] N. J. Ramer and A. M. Rappe, J. Phys. Chem. Solids **61**, 315 (2000).

[18] N. J. Ramer and A. M. Rappe, Phys. Rev. B **62**, 743 (2000).

[19] N. J. Ramer, S. P. Lewis, E. J. Mele, and A. M. Rappe, in *Fundamental Physics of Ferroelectrics 1998, Fifth Williamsburg Workshop*, edited by R. E. Cohen (American Institute of Physics, Woodbury, NY, 1998), pp. 156–64.

[20] S. Teslic and T. Egami, Acta Crystallogr., Sect. B: Struct. Sci. **B54**, 750 (1998).

[21] D. J. Singh, Phys. Rev. B **52**, 12 559 (2001).

[22] A. Garcia and D. Vanderbilt, Appl. Phys. Lett. **72**, 2981 (1998).

[23] L. A. Shuvalov, J. Phys. Soc. Jpn. **28**, 38 (1970).

[24] B. Noheda, Curr. Opin. Solid State Mater. Sci. **6**, 27 (2002).

[25] D. E. Cox, B. Noheda, G. Shirane, Y. Uesu, K. Fujishiro, and Y. Yamada, Appl. Phys. Lett. **79**, 400 (2001).

[26] B. Noheda, D. E. Cox, G. Shirane, J. Gao, and Z. G. Ye, Phys. Rev. B **66**, 054104 (2002).

[27] D. LaOrauttapong, B. Noheda, Z. G. Ye, P. M. Gehring, J. Toulouse, D. E. Cox, and G. Shirane, Phys. Rev. B **65**, 144101 (2002).

[28] T. Egami, W. Dmowski, M. Akbas, and P. K. Davies, in *First-Principles Calculations for Ferroelectrics—Fifth Williamsburg Workshop* (Ref. 19), pp. 1–10.

[29] B. Noheda, L. Wu, and Y. Zhu, Phys. Rev. B **66**, 060103 (2002).

[30] D. M. Hatch, H. T. Stokes, R. Ranjan, S. K. Mishra, D. Pandey, and B. J. Kennedy, Phys. Rev. B **65**, 212101 (2002).

[31] R. Ranjan, S. K. Mishra, D. Pandey, and B. J. Kennedy, Phys. Rev. B **65**, 060102 (2002).

[32] G. W. Watson, S. C. Parker, and G. Kresse, Phys. Rev. B **59**, 8481 (1999).

[33] U. V. Waghmare, N. A. Spaldin, H. C. Kandpal, and R. Seshadri, Phys. Rev. B **67**, 125111 (2003).

[34] R. E. Cohen and H. Krakauer, Phys. Rev. B **42**, 6416 (1990).

[35] R. D. Shannon and C. T. Prewitt, Acta Crystallogr., Sect. B: Struct. Crystallogr. Cryst. Chem. **26**, 1046 (1970).

[36] I. D. Brown, in *Structure and Bonding in Crystals II*, edited by M. O'Keeffe and A. Navrotsky (Academic, New York, 1981), pp. 1–30.

[37] B. P. Burton and E. Cockayne, Phys. Rev. B **60**, 12 542 (1999).

[38] I. Grinberg, V. R. Cooper, and A. M. Rappe, Nature (London) **419**, 909 (2002).

[39] G. O. Jones and P. A. Thomas, Acta Crystallogr., Sect. B: Struct. Sci. **B58**, 168 (2002).

[40] E. Heifets and R. E. Cohen, in *Fundamental Physics of Ferroelectrics 2002*, edited by R. E. Cohen (American Institute of Physics, Melville, NY, 2002), pp. 150–9.

[41] H. Fu and R. E. Cohen, Nature (London) **402**, 281 (2000).

[42] D. M. Ceperley and B. J. Alder, Phys. Rev. Lett. **45**, 566 (1980).

[43] J. P. Perdew and A. Zunger, Phys. Rev. B **23**, 5048 (1981).

[44] A. M. Rappe, K. M. Rabe, E. Kaxiras, and J. D. Joannopoulos, Phys. Rev. B **41**, 1227 (1990).

[45] N. J. Ramer and A. M. Rappe, Phys. Rev. B **59**, 12 471 (1999).

[46] C. Bendtsen, O. H. Nielsen, and L. B. Hansen, Appl. Numer. Math. **37**, 189 (2001).

[47] E. R. Davidson, J. Comput. Phys. **17**, 87 (1975).

[48] P. Pulay, J. Comput. Chem. **3**, 556 (1982).

[49] B. G. Pfrommer, M. Cote, S. G. Louie, and M. L. Cohen, J. Comput. Phys. **131**, 233 (1997).

[50] T. Egami, in *Fundamental Physics of Ferroelectrics—Aspen Center for Physics Winter Workshop*, edited by R. E. Cohen (American Institute of Physics, Melville, NY, 2000), pp. 16–25.

[51] S. J. Zhang, P. W. Rehrig, C. Randall, and T. R. Shrout, J. Cryst. Growth **234**, 415 (2002).

[52] Octahedral volume is computed by multiplying the x, y, and z dimensions of the octahedron.

[53] For a recent review on single crystal relaxor piezoelectrics, see Z.-G. Ye, Curr. Opin. Solid State Mater. Sci. **6**, 35 (2002).